PCCP

ROYAL SOCIETY OF CHEMISTRY

PAPER

Cite this: *Phys. Chem. Chem. Phys.*, 2024, **26**, 25057

Insights into dioxygen binding on metal centers: an *ab initio* multireference electronic structure analysis†

Peng Zhang,[ab] Way-Zen Lee[cd] and Shengfa Ye*[a]

Why does binding of dioxygen (O_2) to metal centers, the initial step of O_2 storage, transportation, and activation, almost inevitably induce metal-to-O_2 single-electron transfer and generate superoxo ($O_2^{-\bullet}$) species, instead of genuine O_2^0 adducts? To address this question, this study describes highly correlated wavefunction-based *ab initio* calculations using CASSCF/NEVPT2 (CASSCF = complete active space self-consistent field, and NEVPT2 = *N*-electron valence state second-order perturbation theory) approaches to explore the electronic-structure evolution of O_2 association on Fe(II)(BDPP) (H_2BDPP = 2,6-bis((2-(*S*)-diphenylhydroxylmethyl-1-pyrrolidinyl)methyl)pyridine) and Co(II)(BDPP) to produce $S = 3$ Fe(III)(BDPP)($O_2^{-\bullet}$) (**1**) and $S = \frac{1}{2}$ Co(III)(BDPP)($O_2^{-\bullet}$) (**2**). CASSCF/NEVPT2 calculations suggest that the processes furnishing **1** and **2** feature an avoided crossing resulting from interactions of two diabatic curves, of which one is characterized as Co(II) and Fe(II) centers interacting with a triplet O_2 ligand and the other as Co(III) and Fe(III) centers bound to a superoxo ligand. In both cases, the avoided crossing induces a one-electron transfer from the divalent metal center to the incoming O_2 ligand and leads to formation of trivalent metal–$O_2^{-\bullet}$ complexes. To facilitate the interpretation of complicated multireference wavefunctions, we formulated two-fragment spin eigenfunctions utilizing Clebsch–Gordan coefficients (CGCs) to rationalize computed spin populations on the metal centers and the O_2 ligand and compared these results with usual valence bonding (VB) analyses. It turns out that both methods give the same results and are complementary to each other. Finally, the limitation of DFT approaches in describing complex electronic structures involving metal–ligand magnetic couplings is delineated.

Received 23rd July 2024,
Accepted 20th August 2024

DOI: 10.1039/d4cp02915a

rsc.li/pccp

Introduction

Binding of dioxygen (O_2) on metal cofactors of metalloproteins initiates a diverse array of physiologically pivotal processes, including O_2 storage, transportation, and activation for substrate functionalization.[1–6] Myoglobin, a heme enzyme containing a high spin ferrous center, reacts with O_2 yielding a singlet O_2 complex,[7–9] while for nonheme enzymes isopenicillin N synthase (IPNS)[10–12] and a variant of homoprotocatechuate 2,3-dioxygenase (Fe-HPCD) with the active site His200 mutated to Asn, labelled as 4-NC,[13] and utilizing an alternative substrate 4-nitrocatechol, O_2 addition results in a quintet O_2 adduct that is best described as a high spin ferric center $\left(S_{\mathrm{Fe}} = \frac{5}{2}\right)$ antiferromagnetically coupled to a superoxo ligand ($O_2^{-\bullet}$) $\left(S_{O_2^{-\bullet}} = \frac{1}{2}\right)$ yielding an overall $S_t = 2$ ground state. To mimic enzymatic O_2 binding, numerous model complexes have been synthesized and characterized.[14,15] The reactions of O_2 with a range of ferrous complexes, such as Fe(II)($\mathrm{BNPA^{Me_2}S}$)(Br) ($\mathrm{BNPA^{Me_2}SH}$ = (bis((6-(neopentylamino)pyridinyl)methyl)amino)-2-methylpropane-2-thiol,[16] ($\mathrm{L^{Ad}H}$)Fe ($\mathrm{L^{Ad}H}$ = tris(phosphinimine) ligand),[17] Fe($\mathrm{S_2^{Me_2}N_3}$(Pr,Pr))[18] and Fe(ttppc) ($\mathrm{ttppc^{3-}}$ = 5,10,15-tris((2,4,6-triphenyl)phenyl)corrolate),[19] all yield similar quintet Fe–O_2 adducts. In contrast to the examples discussed above, treatment of O_2 with a high spin Fe(II) precursor ($S_{\mathrm{Fe}} = 2$), Fe(II)(BDPP) (H_2BDPP = 2,6-bis((2-(*S*)-diphenylhydroxylmethyl-1-pyrrolidinyl)methyl)pyridine), at 193 K generates $S_t = 3$, instead of $S_t = 2$, Fe(III)(BDPP)($O_2^{-\bullet}$) (**1**) attained by a ferromagnetic coupling of a high spin Fe(III) center $\left(S_{\mathrm{Fe}} = \frac{5}{2}\right)$ and a $O_2^{-\bullet}$ ligand $\left(S_{O_2^{-\bullet}} = \frac{1}{2}\right)$.[20] While the corresponding reaction

---

[a] State Key Laboratory of Catalysis, Dalian Institute of Chemical Physics, Chinese Academy of Sciences, Dalian 116023, China
[b] University of Chinese Academy of Sciences, Beijing 100049, China
[c] Department of Chemistry, National Taiwan Normal University, Taipei 11677, Taiwan
[d] Department of Medicinal and Applied Chemistry, Kaohsiung Medical University, Kaohsiung 807, Taiwan

† Electronic supplementary information (ESI) available. See DOI: https://doi.org/10.1039/d4cp02915a

with high spin Co(II)(BDPP)[21] $\left(S_{\mathrm{Co}}=\frac{3}{2}\right)$ at 193 K furnishes a doublet Co(III)–$O_2^{-\bullet}$ species, Co(III)(BDPP)($O_2^{-\bullet}$) (**2**), which has been characterized as consisting of a low spin Co(III) center (S_{Co} = 0) interacting with a superoxo ligand $\left(S_{O_2^{-\bullet}}=\frac{1}{2}\right)$.[22] Furthermore, the same product was also found for O_2 addition to Co-HPCD,[23] the Co derivative of Fe-HPCD, and a plethora of high spin or low spin Co(II) complexes, including Co-TPP (TPP^{2-} = tetraphenylporphyrinate),[24] Co(Me_3TACN)(S_2SiMe_2) (Me_3TACN = 1,4,7-trimethyl-1,4,7-triazacyclononane),[25] Co(Tp^{Me_2})($^{t\mathrm{Bu}2}$APH) (Tp^{Me_2} = hydrotris(3,5-dimethylpyrazolyl)borate,[26] $^{t\mathrm{Bu}2}$APH = 2-amino-4,6-di-*tert*-butylphenol), Co(salen)[27] and Co(Por) (Por = porphyrin).[28] Over-decade intensive investigations revealed that O_2 association on divalent nonheme metal centers almost inevitably entails a metal-to-O_2 electron transfer and thus produces a trivalent metal–$O_2^{-\bullet}$ complex.[29,30] To the best of our knowledge, there is only one exception; O_2 binding on a variant of Fe-HPCD labelled as Y257F-HPCA was proposed to form an Fe(II)–O_2 intermediate, instead of Fe(III)–$O_2^{-\bullet}$.[31–35] An intriguing question thus arises about whether it is viable to generate such an authenticated O_2 adduct from O_2 association on metal centers.

In parallel to intensive experimental research, a great deal of computational studies have been devoted to probing electronic structures of O_2 adducts and evaluating electronic-structure evolution over the course of O_2 binding processes.[36–44] In this regard, density functional theory (DFT) calculations usually cannot yield satisfactory results, especially for those systems featuring antiferromagnetic coupling of two fragments. In principle, such a complicated electronic structure cannot be appropriately described by a single Slater determinant. Consequently, broken symmetry formalism has to be invoked, because of the inherent single determinant restriction of DFT approaches.[45] The Kohn–Sham solution thus obtained is no longer the eigenfunction of $\hat{S}^2$; consequently, the resulting spin density is not correct, and the subsequent spin population analysis is physically unjustified. To obtain more accurate electronic structures, one has to resort to highly correlated wavefunction-based multireference approaches.[36–38,42,44] To date, these methods have been successfully applied to O_2 adducts of heme systems, but hardly to nonheme ones.[30] To the best of our knowledge, only one *ab initio* study has been reported thus far where potential energy curves of varying spin states were computed for O_2 association on a heme center.[46] This work does not focus on the elucidation of electronic-structure changes occurring during this process but on the quintet-to-singlet spin crossover; hence, it does not provide sufficient information to address the aforementioned question.

In the present work, we describe a detailed multireference analysis of the electronic-structure evolution as O_2 steadily approaches the Fe(II) and Co(II) centers in Fe(II)(BDPP) and Co(II)(BDPP) affording **1** and **2**, respectively. Specifically, highly correlated wavefunction-based complete active space self-consistent field (CASSCF)[47]/*N*-electron valence state second-order perturbation theory (NEVPT2)[48,49] computations were carried out on a series of geometric structures on the reaction trajectory generated by DFT computations. To interpret complicated multireference wavefunctions of O_2 adducts, we constructed two-fragment spin eigenfunctions using Clebsch–Gordan coefficients (CGCs)[50] to rationalize computed spin populations. CASSCF/NEVPT2 calculations suggest that the O_2 binding processes furnishing **1** and **2** feature an avoided crossing of two diabatic curves that represent the limiting valence structures of Fe(II)/Co(II)–O_2^0 and Fe(III)/Co(III)–$O_2^{-\bullet}$. Their interaction induces a spontaneous single-electron transfer from the divalent metal center to the incoming O_2 ligand, thereby leading to the formation of trivalent metal–$O_2^{-\bullet}$ complexes as the final product for the O_2 binding processes.

Computation setup

To obtain the reaction trajectory for the formation of complexes **1** and **2**, the M–O_2 distance steadily varied from 1.75 to 4.50 Å in an S = 3 and an $S=\frac{1}{2}$ state, respectively, in relaxed surface scans conducted by using the B3LYP functional[51,52] in conjunction with the def2-TZVP basis set[53–55] for N, O, Fe, and Co, and the def2-SVP basis set[56,57] for the other atoms (C and H atoms). Moreover, RIJCOSX approximations[58] were employed in combination with the def2/J auxiliary basis set[59,60] to speed up DFT computations. To take solvation effects into consideration, the CPCM model[61] with THF as the solvent was applied, and D3BJ corrections[62,63] were used to account for dispersion corrections. Frequency analysis on a given optimized geometry structure was performed to compute its zero point energy (ZPE) and thermal corrections. To compute reliable electronic structures, CASSCF calculations using the def2-TZVP basis set for all atoms were carried out at each geometric structure of the reaction trajectory. As verified below, the appropriate active spaces of complexes **1** and **2** were chosen to distribute 12 and 13 electrons, respectively, into 9 orbitals including five metal 3d-based orbitals (five spherical 3d orbitals are used here), two O_2 π bonding (π_{ip} and π_{op}) and the corresponding π* antibonding $\left(\pi_{\mathrm{ip}}^*\text{ and }\pi_{\mathrm{op}}^*\right)$ orbitals. For complex **1**, CASSCF calculations averaged a triplet, a quintet, and a septet state, and for complex **2**, a doublet, a quartet, and a sextet state were considered. Based on the converged state-average CASSCF wavefunction, complete active space configuration interaction (CASCI) calculations were employed to calculate spin density and spin populations of a specific spin state. On top of CASSCF wavefunctions, NEVPT2 computations were undertaken to obtain more precise electronic energies. To accelerate *ab initio* computations, RIJK approximations[64] in conjunction with the def2/JK auxiliary basis set[65] were used. Thus, the final potential energy surface was constructed by using the electronic energy derived from CASSCF/NEVPT2 calculations combined with the ZPE contribution and thermal corrections. All computations were performed using the ORCA-5.0.3 program package.[66]

Results and discussion

Choice of active spaces

Unlike DFT, CASSCF is not a black box method. As the first step to initiate CASSCF calculations, one should prudently select a proper active space,[67] for which some preliminary understanding is required of the electronic structure of the system under investigation. To ensure that the chosen active space is sufficient to provide reliable electronic structures, further calculations are often necessary with enlarged and/or truncated active spaces. Critically, CASSCF computations with suitable active spaces not only yield precise electronic structures but also result in fast convergence. Usually, because d and f orbitals of transition metal compounds are nearly degenerate which leads to strong multiconfiguration character, these orbitals should be included in the active space. Equally important is that to properly describe a metal–ligand covalent bond, the active space ought to contain its bonding and antibonding molecular orbitals (MOs). Otherwise, the CASSCF computations with an unbalanced active space would result in an incorrect electronic structure. Both criteria were used to choose a suitable active space for our CASSCF calculations.

In the present case, in addition to 5 metal 3d-based orbitals, two π bonding (π_{ip} and π_{op}) and two π* antibonding $\left(\pi^*_{ip}\text{ and }\pi^*_{op}\right)$ orbitals of the O_2 ligand should be included in the active space. As elaborated below, this active space can properly describe the metal–O_2 covalent bonding built from the metal 3d and O_2 π* fragment orbitals of appropriate symmetry. Therefore, the active spaces of complexes **1** and **2** were chosen to distribute 12 and 13 electrons, respectively, in 9 orbitals. Depicted in Fig. 1 is the active space of complex **2** obtained by the CASSCF(13,9) computation at the Co–O_2 bond length of 2.50 Å. An analogous active space was employed for complex **1**.

To test the appropriateness of the selected active space, we took complex **2** at the Co–O_2 bond length of 2.50 Å as an example and performed a series of CASSCF computations with different active spaces. First, we added $BDPP^{2-}$ O and N 2p donor based σ_{eq} into the active space that is the σ bonding counterpart with respect to $d_{x^2-y^2}$. Accordingly, two more electrons ought to be added into the active space, thereby resulting in an active space of CAS(15,10). Second, we constructed an active space of CAS(15,11) that includes O_2 σ and σ* orbitals to take the entire 2p shells of the O_2 moiety into consideration. Third, an even larger active space of CAS(17,12) was built up to encompass all the aforementioned effects. As summarized in Table 1, the occupation numbers of σ_{eq} are invariably 2 for all key electron configurations of each spin state derived from CASSCF(15,10) calculations. Similarly, the occupation numbers of O_2 σ and σ* remain constants at 2 and 0, respectively, for all important electron configurations predicted by CASSCF(15,11) computations. Both findings hold true for the CASSCF(17,12) results. As such, for a given spin state, all CASSCF computations give qualitatively the same electronic structures as evidenced by almost identical percentage of each dominant electron configuration and hence spin populations on the Co center and the O_2 moiety. Moreover, we have also performed CASSCF calculations with these three distinct active spaces on complex **2** at a longer (4.50 Å) and a shorter (1.91 Å) Co–O_2 bond length, and again the calculations produced analogous results, as shown in Fig. S1 and S2 (ESI†). In addition, we have also carried out CASSCF(13,9) calculations using different basis sets, such as def2-SV, def2-SVP, def2-TZVP and def2-TZVPP, and the same electronic structures were obtained as listed in Tables S1–S3 (ESI†). In summary, the active space of CAS(13,9) combined with the def2-TZVP basis set is sufficient to yield reliable electronic structures and bonding features for complex **2** at varying Co–O_2 bond distances. Likewise, CASSCF(12,9) with the def2-TZVP basis set should produce satisfactory results for the O_2 association process affording complex **1** as well.

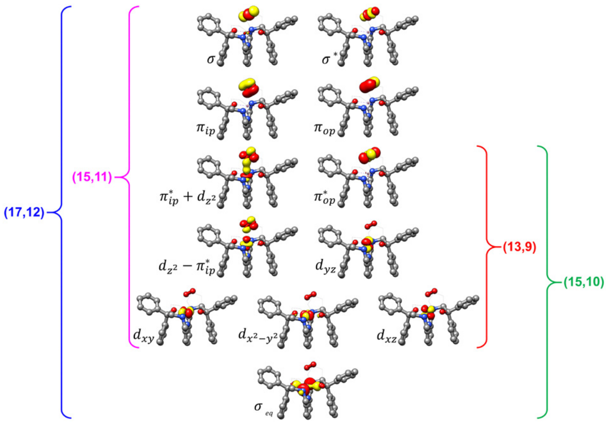

Fig. 1 Different choices of active spaces (*m*,*n*) (*m* electrons in *n* orbitals) for complex **2** at the Co–O_2 bond length of 2.50 Å. For clarity, hydrogen atoms are omitted for clarity.

O_2 binding on Fe(II)(BDPP) affording complex 1

Depicted in Fig. 2 is the $S_t = 3$ potential energy surface of O_2 bonding to high spin Fe(II)(BDPP) calculated using CASSCF(12,9)/NEVPT2 computations. As expected, starting point ^{7}**A** with a Fe–O_2 bond length of 4.00 Å is best interpreted as a high spin Fe(II) ion ($S_{Fe} = 2$) ferromagnetically coupled with a triplet O_2 ligand ($S_{O_2} = 1$) yielding an overall septet state. Consistent with this assignment, *ab initio* calculations indicate that this state is distinguished by a leading electron configuration of $d_{xz}{}^2 d_{yz}{}^1 d_{xy}{}^1 d_{x^2-y^2}{}^1 d_{z^2}{}^1 \pi_{ip}{}^2 \pi_{op}{}^2 \pi^{*1}_{ip} \pi^{*1}_{op}$ (95%). As shown in Fig. 2, the computed spin density and spin populations (Löwdin analysis, 3.86 for Fe and 2.00 for O_2; Mulliken analysis, 3.91 for Fe and 2.00 for O_2) further corroborate this electronic-structure formulation. Of note, because spin populations estimated by Löwdin and Mulliken analyses are essentially the same, in the following section, we only discuss the former but list the latter in Fig. 2. As the O_2 ligand steadily approaches the Fe center, the energy of this valence structure invariably rises as shown by the corresponding diabatic potential curve (magenta line). During this process, the nature of the Fe–O_2 bonding remains essentially the same as indicated by the unchanged

Table 1 Spin populations on the Co center and O_2 moiety and electron configurations for each spin state from CASSCF calculations with different choices of active orbitals for complex **2** at the Co–O_2 bond length of 2.50 Å

	Configuration			Spin populations		
	Sextet	Quartet	Doublet	Sextet	Quartet	Doublet
CASSCF(13,9) $d_{xz}d_{yz}d_{xy}d_{x^2-y^2}\left(d_{z^2}-\pi^*_{ip}\right)\pi_{op}\pi_{ip}\pi^*_{op}\left(\pi^*_{ip}+d_{z^2}\right)$	87% 221112211	42% 221112211 14% 221102212 10% 221122210 9% 221012212 6% 221212210	21% 221112211 21% 221102212 14% 221122210 13% 221012212 9% 221212210	Co 2.83 (2.88) O_2 1.98 (2.00)	Co 2.08 (2.11) O_2 0.79 (0.80)	Co 1.56 (1.59) O_2 −0.65 (−0.66)
CASSCF(15,10) $\sigma_{eq}d_{xz}d_{yz}d_{xy}d_{x^2-y^2}\left(d_{z^2}-\pi^*_{ip}\right)\pi_{op}\pi_{ip}\pi^*_{op}\left(\pi^*_{ip}+d_{z^2}\right)$	87% 2221112211	43% 2221112211 15% 2221102212 10% 2221122210 8% 2221012212 5% 2221212210	22% 2221112211 22% 2221102212 15% 2221122210 11% 2221012212 8% 2221212210	Co 2.83 (2.88) O_2 1.98 (1.99)	Co 2.08 (2.11) O_2 0.79 (0.80)	Co 1.56 (1.59) O_2 −0.65 (−0.66)
CASSCF(15,11) $d_{xz}d_{yz}d_{xy}d_{x^2-y^2}\left(d_{z^2}-\pi^*_{ip}\right)\pi_{op}\pi_{ip}\pi^*_{op}\left(\pi^*_{ip}+d_{z^2}\right)\sigma\sigma^*$	87% 22111221120	46% 22111221120 19% 22110221220 13% 22112221020 3% 22101221220 2% 22121221020	20% 22111221120 30% 22110221220 21% 22112221020 5% 22101221220 4% 22121221020	Co 2.83 (2.88) O_2 1.98 (1.99)	Co 2.07 (2.11) O_2 0.80 (0.80)	Co 1.56 (1.59) O_2 −0.65 (−0.66)
CASSCF(17,11) $\sigma_{eq}d_{xz}d_{yz}d_{xy}d_{x^2-y^2}\left(d_{z^2}-\pi^*_{ip}\right)\pi_{op}\pi_{ip}\pi^*_{op}\left(\pi^*_{ip}+d_{z^2}\right)\sigma\sigma^*$	87% 222111221120	47% 222111221120 19% 222110221220 13% 222112221020 3% 222101221220 2% 222121221020	21% 222111221120 31% 222110221220 21% 222112221020 5% 222101221220 3% 222121221020	Co 2.83 (2.88) O_2 1.98 (1.99)	Co 2.07 (2.11) O_2 0.80 (0.80)	Co 1.56 (1.59) O_2 −0.65 (−0.66)

spin populations on the Fe(II) center and the O_2 ligand, for instance, complex ^{7}**B**. However, starting from the Fe–O_2 distance of 2.30 Å, CASSCF(12,9) calculations could converge to another solution as exemplified by complex ^{7}**1**. It features a sole electron configuration of $d_{xz}{}^{1}\left(d_{yz}+\pi^*_{op}\right)^{1}d_{xy}{}^{1}d_{x^2-y^2}{}^{1}\left(d_{z^2}-\pi^*_{ip}\right)^{1}\pi_{ip}{}^{2}\pi_{op}{}^{2}\left(\pi^*_{ip}+d_{z^2}\right)^{2}\left(\pi^*_{op}-d_{yz}\right)^{1}$ (100%) and is best described as a high spin Fe(III) center $\left(S_{Fe}=\frac{5}{2}\right)$ ferromagnetically coupled with a superoxo ligand $\left(S_{O_2^{-}\bullet}=\frac{1}{2}\right)$ as suggested by the computed spin density and spin populations (4.74 for Fe and 1.03 for O_2). Its energy first descends for the Fe–O_2 distance lowering from 2.30 Å to 2.06 Å and then ascends as the Fe–O_2 distance further decreases; thus, its diabatic potential curve (crimson curve) displays a local minimal (^{7}**1**) at a Fe–O_2 distance of ∼2.00 Å.

The interaction of the aforementioned two diabatic potential curves results in an avoided crossing near the Fe–O_2 bond length of 2.30 Å and a barrier of 13.6 kcal mol^{-1}. Moreover, the entire process is moderately endothermic with a driving force of 8.0 kcal mol^{-1}. This value should be somewhat overestimated by our computations, because experimentally ^{7}**1** is stable at low temperatures (<193 K) but releases O_2 affording Fe(II)(BDPP) upon raising the temperature. The overestimation of the binding barrier can be ascribed to the fact that the active space employed does not suffice to capture escalating electron correlations at the transition state where two diabatic surfaces strongly interact. Nevertheless, the entire process can be interpreted as shifting one β electron from the Fe d_{xz} orbital to the O_2 π^*_{ip} orbital, thus leading to the formation of ^{7}**1**. As indicated by the septet potential surface, because in the avoided crossing region an energetically favorable electron transfer from the Fe(II) center to the O_2 ligand takes place, which allows the system to ultimately convert into ^{7}**1**, it is unlikely to trap the proposed Fe(II)–O_2 complex during this O_2 binding process. In line with this prediction, UV-vis measurements at 193 K showed that no intervening intermediate could be detected en route to ^{7}**1**.[20]

Experimentally, the O_2 adducts of IPNS[10–12] and the 4-NC variant of Fe-HPCD[13] have been spectroscopically identified to be quintet Fe(III)-superoxo species. However, our CASSCF(12,9)/NEVPT2 computations could not allow to determine the exact ground state of complex **1** because the estimated septet–quintet energy gap of 2.4 kcal mol^{-1} falls within the range of uncertainty for *ab initio* calculations. Thus, we also investigated the reaction of Fe(II)(BDPP) with O_2 in an S_t = 2 state. As shown in Fig. 2, the quintet potential energy surface computed for the O_2 binding process is essentially parallel to the septet one in the sense that there exists an analogous avoided crossing around the Fe–O_2 distance of 2.30 Å derived from interactions of two diabatic potential curves, yielding a barrier of 11.3 kcal mol^{-1}. Furthermore, the quintet reaction also entails a comparable driving force of 5.6 kcal mol^{-1}. As elaborated below, the diabatic potential curve starting with complex ^{5}**A** describes the energy variation of an S_t = 2 state attained by a magnetic coupling of a high spin Fe(II) center (S_{Fe} = 2) and a triplet O_2 ligand (S_{O_2} = 1) as a function of the Fe–O_2 distance; the other one represents a high spin Fe(III) center $\left(S_{Fe}=\frac{5}{2}\right)$ antiferromagnetically coupled with a doublet superoxo ligand $\left(S_{O_2^{-}\bullet}=\frac{1}{2}\right)$.

Ab initio calculations reveal that complex ^{5}**A** is isoenergetic to ^{7}**A** and, importantly, the leading electron configuration

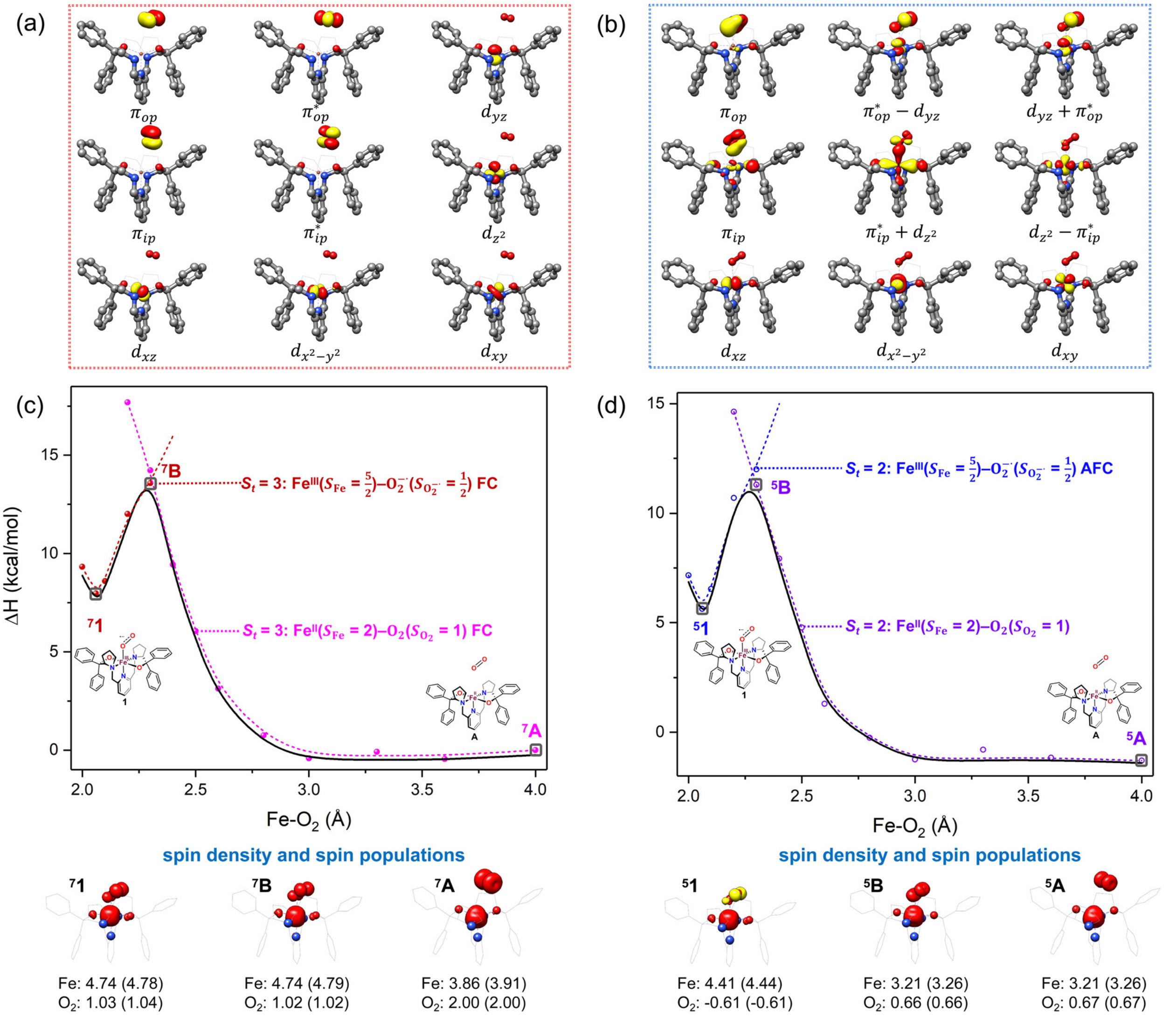

Fig. 2 Active spaces of complexes **A** (a) and **1** (b); septet potential energy surface for the reaction of Fe(II)(BDPP) with O$_2$ as a function of the Fe–O$_2$ bond distance obtained from CASSCF(12,9)/NEVPT2 computations; dot lines denote diabatic potential curves (magenta line denotes an S_t = 3 Fe^{II}–O$_2$ complex consisting of as an S_{Fe} = 2 Fe^{II} center ferromagnetically coupled (FC) with an S_{O_2} = 1 O$_2$ ligand; the crimson line denotes an S_t = 3 Fe^{III}–O$_2^{-\bullet}$ complex consisting of an $S_{Fe} = \frac{5}{2}$ Fe^{III} center ferromagnetically coupled (FC) with an $S_{O_2^-\bullet} = \frac{1}{2}$ O$_2^{-\bullet}$ ligand) and the black line denotes an adiabatic curve for the reaction on the S = 3 potential surface; spin density and Löwdin and Mulliken (in parentheses) spin populations on the Fe center and the O$_2$ unit calculated for complexes ^{7}**A** (Fe(II)(BDPP) + O$_2$), ^{7}**B**, and ^{7}**1** on the reaction trajectory are shown at the bottom, yellow and red denote negative and positive spin density, respectively, and local spin populations are also listed in the ESI† (c); the quintet potential energy surface for the reaction of Fe(II)(BDPP) with O$_2$ as a function of the Fe–O$_2$ bond distance obtained from CASSCF(12,9)/NEVPT2 computations; the dot lines denote diabatic potential curves (violet line denotes a quintet state Fe^{II}–O$_2$ complex, interpreted as an S_{Fe} = 2 Fe^{II} compound magnetically coupled with an S_{O_2} = 1 O$_2$ ligand; the blue line denotes a quintet state Fe^{III}–O$_2^{-\bullet}$ complex, interpreted as an $S_{Fe} = \frac{5}{2}$ Fe^{III} center antiferromagnetically coupled (AFC) with an $S_{O_2^-\bullet} = \frac{1}{2}$ O$_2^{-\bullet}$ ligand) and the black lines denote adiabatic curves for the reaction on the S = 2 potential surface; spin density and Löwdin and Mulliken (in parentheses) spin populations on the Fe center and O$_2$ unit calculated for complexes ^{5}**A** (Fe(II)(BDPP) + O$_2$), ^{5}**B**, and ^{5}**1** on the reaction trajectory are shown at the bottom, yellow and red denote negative and positive spin density, respectively, and local spin populations are also listed in the ESI† (d); hydrogen atoms are omitted for clarity.

$d_{xz}^2 d_{yz}^1 d_{xy}^1 d_{x^2-y^2}^1 d_{z^2}^1 \pi_{ip}^2 \pi_{op}^2 \pi_{ip}^{*1} \pi_{op}^{*1}$ (94%) of the former species is also the same as that of the latter. This can be traced back to the large Fe–O$_2$ separation that prevents any non-negligible metal–ligand interactions from occurring. Following this line of reasoning, ^{5}**A** should contain a quintet Fe(II) center (S_{Fe} = 2) that is exchange coupled to a triplet O$_2$ ligand (S_{O_2} = 1). However, the spin populations calculated for the Fe center (3.21) and the O$_2$ ligand (0.67) differ significantly from those expected for non-interacting S_{Fe} = 2 Fe(II) and S_{O_2} = 1 O$_2$ fragments. To solve this problem, the vector coupling model was invoked to construct the spin eigenfunction with a well-defined total spin S of the resulting state derived from the magnetic coupling of a high spin Fe(II) center and a triplet O$_2$ ligand using CGCs. In the present case, the former entity can be characterized by spin eigenfunction $|S_1,M_1\rangle = |2,M_1\rangle$ ($M_1 = \pm2, \pm1, 0$), and the latter by $|S_2,M_2\rangle = |1,M_2\rangle$ ($M_2 = \pm1, 0$). The quintet state originating from the interaction of these two fragments should be distinguished by spin eigenfunction $|S,M\rangle = |2,M\rangle$ ($M = \pm2, \pm1, 0$), and its standard component reads $|2,2\rangle = \sqrt{\frac{2}{3}}|2,2|1,0\rangle - \sqrt{\frac{1}{3}}|2,1|1,1\rangle$, where the functions on the right hand of the equal sign are written as $|S_1,M_1|S_2,M_2\rangle$. This spin eigenfunction features $\hat{S}_z$ expectation values (the spin projection along the z axis) of $\frac{5}{3}$ and $\frac{1}{3}$ for the Fe(II) center and the O_2 unit, respectively. Indeed, both values are in line with the computed spin populations (3.21 for Fe and 0.67 for O_2), because ideally spin populations are twice the $\hat{S}_z$ expectation values, thus affirming the proposed electronic-structure assignment.

Regarding the O_2 binding process furnishing ^{5}**1**, as the Fe–O_2 distance decreases from 4.00 Å to 2.30 Å (violet curve), the wavefunction steadily acquires multireference character having three dominant electron configurations of $\mathrm{d}_{xz}{}^2\mathrm{d}_{yz}{}^1\mathrm{d}_{xy}{}^1\mathrm{d}_{x^2-y^2}{}^1\left(\mathrm{d}_{z^2}-\pi^*_{\mathrm{ip}}\right)^1\pi_{\mathrm{ip}}{}^2\pi_{\mathrm{op}}{}^2\left(\pi^*_{\mathrm{ip}}+\mathrm{d}_{z^2}\right)^1\pi^{*1}_{\mathrm{op}}$, $\mathrm{d}_{xz}{}^2\mathrm{d}_{yz}{}^1\mathrm{d}_{xy}{}^1\mathrm{d}_{x^2-y^2}{}^1\left(\mathrm{d}_{z^2}-\pi^*_{\mathrm{ip}}\right)^0\pi_{\mathrm{ip}}{}^2\pi_{\mathrm{op}}{}^2\left(\pi^*_{\mathrm{ip}}+\mathrm{d}_{z^2}\right)^2\pi^{*1}_{\mathrm{op}}$, and $\mathrm{d}_{xz}{}^2\mathrm{d}_{yz}{}^1\mathrm{d}_{xy}{}^1\mathrm{d}_{x^2-y^2}{}^1\left(\mathrm{d}_{z^2}-\pi^*_{\mathrm{ip}}\right)^2\pi_{\mathrm{ip}}{}^2\pi_{\mathrm{op}}{}^2\left(\pi^*_{\mathrm{ip}}+\mathrm{d}_{z^2}\right)^0\pi^{*1}_{\mathrm{op}}$. These three electron configurations differ in their varying occupation numbers in $\pi^*_{\mathrm{ip}}+\mathrm{d}_{z^2}$ and $\mathrm{d}_{z^2}-\pi^*_{\mathrm{ip}}$ orbitals, both of which, in fact, describe the covalent interaction between the Fe(II) center and the O_2 ligand (Fig. 1). During this process, the weight of the first one plummets from 94% to 57%, while those of the last two rise from 0% to 21% and 12%, respectively, likely suggesting the progressively strengthened covalent Fe–O_2 interaction. However, the spin density and spin populations computed for ^{5}**B** are analogous to those for ^{5}**A**. This finding demonstrates that the electronic structure of ^{5}**B** is nearly the same as that of ^{5}**A**, indicative of weak covalent Fe–O_2 interaction of ^{5}**B**. As the Fe–O_2 bond length further declines, one electron is shifted from the Fe(II) center to the O_2 ligand near the avoided crossing region accompanied by a rapid adjustment of the electronic structure of the nascent Fe(III) center to afford ^{5}**1** in the end.

CASSCF(12,9) calculations reveal that the quintet state of complex ^{5}**1** features strong multireference character and consists of three key electron configurations of $\mathrm{d}_{xz}{}^1\left(\mathrm{d}_{yz}+\pi^*_{\mathrm{op}}\right)^1\mathrm{d}_{xy}{}^1\mathrm{d}_{x^2-y^2}{}^1\left(\mathrm{d}_{z^2}-\pi^*_{\mathrm{ip}}\right)^1\pi_{\mathrm{ip}}{}^2\pi_{\mathrm{op}}{}^2\left(\pi^*_{\mathrm{ip}}+\mathrm{d}_{z^2}\right)^2\left(\pi^*_{\mathrm{op}}-\mathrm{d}_{yz}\right)^1$ (39%), $\mathrm{d}_{xz}{}^1\left(\mathrm{d}_{yz}+\pi^*_{\mathrm{op}}\right)^0\mathrm{d}_{xy}{}^1\mathrm{d}_{x^2-y^2}{}^1\left(\mathrm{d}_{z^2}-\pi^*_{\mathrm{ip}}\right)^1\pi_{\mathrm{ip}}{}^2\pi_{\mathrm{op}}{}^2\left(\pi^*_{\mathrm{ip}}+\mathrm{d}_{z^2}\right)^2\left(\pi^*_{\mathrm{op}}-\mathrm{d}_{yz}\right)^2$ (30%), and $\mathrm{d}_{xz}{}^1\left(\mathrm{d}_{yz}+\pi^*_{\mathrm{op}}\right)^2\mathrm{d}_{xy}{}^1\mathrm{d}_{x^2-y^2}{}^1\left(\mathrm{d}_{z^2}-\pi^*_{\mathrm{ip}}\right)^1\pi_{\mathrm{ip}}{}^2\pi_{\mathrm{op}}{}^2\left(\pi^*_{\mathrm{ip}}+\mathrm{d}_{z^2}\right)^2\left(\pi^*_{\mathrm{op}}-\mathrm{d}_{yz}\right)^0$ (27%). Apparently, this wavefunction is too complex to extract any chemically sensible bonding information from its predominant electron configurations. Specifically, the first one could be interpreted as a high spin Fe(III) center $\left(S_{\mathrm{Fe}}=\frac{5}{2}\right)$ antiferromagnetically coupled to a doublet superoxo ligand $\left(S_{O_2^{-}\bullet}=\frac{1}{2}\right)$, the second one as a quintet Fe(IV) center ($S_{\mathrm{Fe}} = 2$) bound to a singlet peroxo ligand ($S_{O_2^{2-}} = 0$), and the last one as a high spin Fe(II) center ($S_{\mathrm{Fe}} = 2$) coordinated by a singlet O_2 ligand ($S_{O_2} = 0$). However, as demonstrated in Fig. 2, the spin density calculated for complex ^{5}**1** exhibits a spherical shape for the Fe center, reminiscent of the high spin Fe(III) center $\left(S_{\mathrm{Fe}}=\frac{5}{2}\right)$ in complexes ^{7}**B** and ^{7}**1**, but different from the high spin Fe(II) center ($S_{\mathrm{Fe}} = 2$) in complexes ^{7}**A** and ^{5}**A**. Moreover, the spin density reveals substantial negative spin primarily populating the O_2 π^*_{op} orbital, thereby signaling that the O_2 ligand is best described as a doublet superoxo ligand $\left(S_{O_2^{-}\bullet}=\frac{1}{2}\right)$. Based on these findings, we surmised that complex ^{5}**1** is best described as a high spin Fe(III) center $\left(S_{\mathrm{Fe}}=\frac{5}{2}\right)$ antiferromagnetically coupled with a superoxo ligand $\left(S_{O_2^{-}\bullet}=\frac{1}{2}\right)$ affording an overall $S_t = 2$ state. Following the route used to interpret the electronic structure of ^{5}**A**, such a bonding situation should be described by $|2,2\rangle = \sqrt{\frac{5}{6}}\left|\frac{5}{2},\frac{5}{2}\middle|\frac{1}{2},-\frac{1}{2}\right\rangle - \sqrt{\frac{1}{6}}\left|\frac{5}{2},\frac{3}{2}\middle|\frac{1}{2},\frac{1}{2}\right\rangle$. This spin eigenfunction furnishes $\hat{S}_z$ expectation values of $\frac{7}{3}$ and $-\frac{1}{3}$ for the Fe center and the O_2 ligand, respectively, congruent with the computed spin populations (4.41 for Fe and −0.61 for O_2), affirming the bonding interpretation.

Alternatively, to interpret the multireference wavefunction computed for complex ^{5}**1**, valence bonding (VB) reading[68–71] was also employed as exemplified by the VB analysis of the electronic structure of the myoglobin O_2 adduct reported by Sason and coworkers.[72] As shown in Fig. 3, upon localization of $\mathrm{d}_{yz}+\pi^*_{\mathrm{op}}$ and $\pi^*_{\mathrm{op}}-\mathrm{d}_{yz}$, representing bonding and antibonding interactions of d_{yz} and π^*_{op}, the ground state wavefunction re-expressed in the basis of the localized orbitals (d_{yz} and π^*_{op}) contains merely one electron configuration of $\mathrm{d}_{xz}{}^1\mathrm{d}_{yz}{}^1\mathrm{d}_{xy}{}^1\mathrm{d}_{x^2-y^2}{}^1\mathrm{d}_{z^2}{}^1\pi_{\mathrm{ip}}{}^2\pi_{\mathrm{op}}{}^2\pi^{*2}_{\mathrm{ip}}\pi^{*1}_{\mathrm{op}}$ (99%), whereas the original one in the basis of the natural orbitals exhibits strong multireference character having three dominant electron configurations as discussed above. It should be pointed out that both wavefunctions are equivalent because they are related by a unitary transformation of orbitals in the active space. Moreover, the computed spin density and spin populations reveal that the majority spin is located on the Fe center and the minority one of the opposite sign on the O_2 ligand. As such, the spin-up and spin-down electrons, which are spin paired, are located in the d_{yz} and π^*_{op} MOs, respectively. Both findings therefore approve of the electronic-structure assignment presented above.

Clearly, in the case of complex ^{5}**1**, VB analyses is as efficient as constructing two-fragment spin eigenfunction in interpreting its multireference wavefunction. However, this approach is not applicable to complex ^{5}**A** where the absence of any covalent interactions between the Fe center and the O_2 ligand renders localization fruitless. It follows that VB analysis cannot be used to characterize multireference wavefunctions without strong electron correlations. In this respect, our simple approach does not have such a limitation.

The reaction of Fe(II)(BDPP) with O_2 in an S_t = 1 state also features two diabatic potential curves, one denotes a high spin Fe(II) center (S_{Fe} = 2) antiferromagnetically coupled with a triplet O_2 ligand (S_{O_2} = 1), and the other describes an intermediate spin Fe(III) center $\left(S_{Fe}=\frac{3}{2}\right)$ antiferromagnetically coupled with a doublet superoxo ligand $\left(S_{O_2^{-}\bullet}=\frac{1}{2}\right)$. Although the triplet transformation is barrierless, it is highly endothermic by 30.2 kcal mol^{-1}. (See the ESI† for more details) and cannot contribute to the actual reaction. Taken together, O_2 association on a high spin ferrous center proceeds either on a septet or on a quintet surface, in line with the experimental findings.[20]

O_2 binding on Co(II)(BDPP) affording complex 2

As shown in Fig. 4, starting from ^{2}**C** at a Co–O_2 distance of 4.50 Å, the diabatic potential curve (magenta line) of the doublet state arising from an antiferromagnetic coupling of a

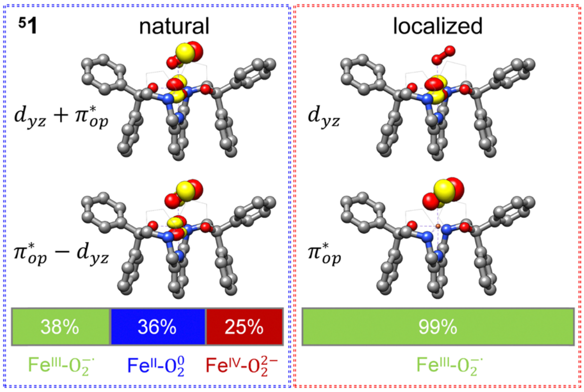

Fig. 3 d_{yz} and π^*_{op} MOs in natural and localized forms with the electron configurations and their weights for ^{5}**1** complex; Fe^{III}–O$_2$$^{-\bullet}$ denotes the electron configuration of $d_{xz}{}^1\left(d_{yz}+\pi^*_{op}\right)^1 d_{xy}{}^1 d_{x^2-y^2}{}^1\left(d_{z^2}-\pi^*_{ip}\right)^1 \pi_{ip}{}^2\pi_{op}{}^2 \left(\pi^*_{ip}+d_{z^2}\right)^2\left(\pi^*_{op}-d_{yz}\right)^1$, Fe^{IV}–O$_2$$^{2-}$ represents the electron configuration of $d_{xz}{}^1\left(d_{yz}+\pi^*_{op}\right)^0 d_{xy}{}^1 d_{x^2-y^2}{}^1\left(d_{z^2}-\pi^*_{ip}\right)^1 \pi_{ip}{}^2\pi_{op}{}^2\left(\pi^*_{ip}+d_{z^2}\right)^2\left(\pi^*_{op}-d_{yz}\right)^2$, and Fe^{II}–O$_2$ indicates the electron configuration of $d_{xz}{}^1\left(d_{yz}+\pi^*_{op}\right)^2 d_{xy}{}^1 d_{x^2-y^2}{}^1\left(d_{z^2}-\pi^*_{ip}\right)^1 \pi_{ip}{}^2\pi_{op}{}^2\left(\pi^*_{ip}+d_{z^2}\right)^2\left(\pi^*_{op}-d_{yz}\right)^0$, and hydrogen atoms are omitted for clarity.

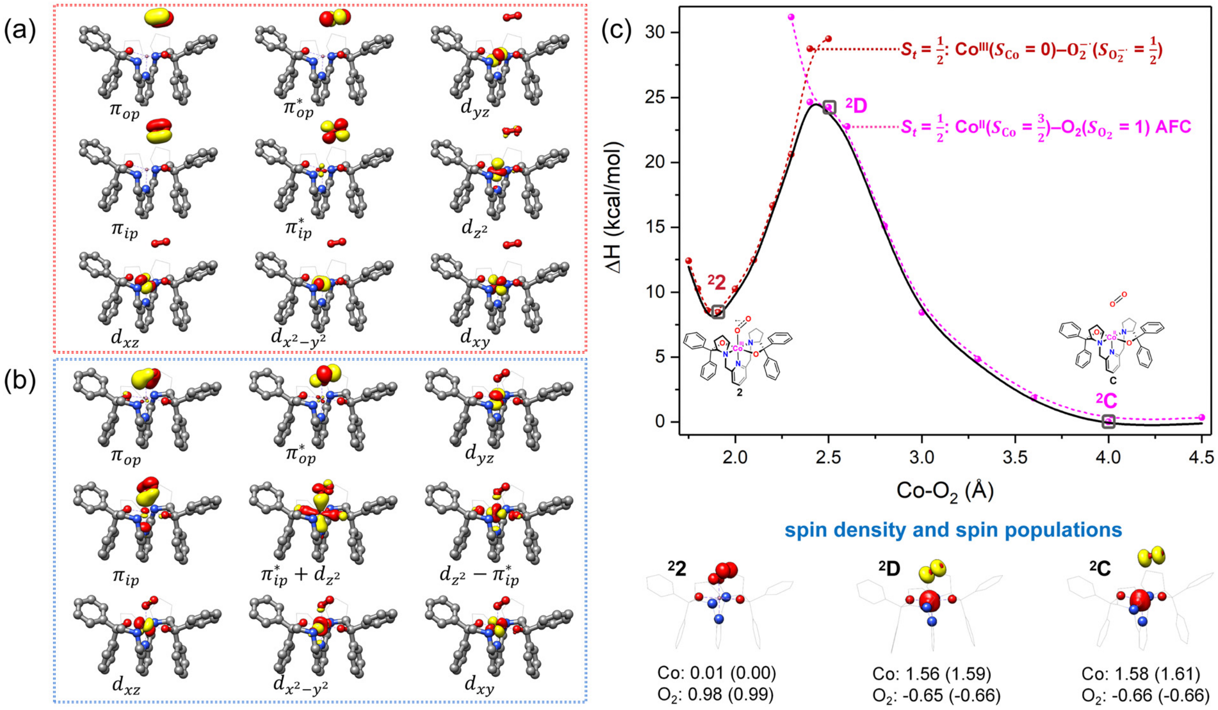

Fig. 4 Active spaces of complexes **C** (a) and **2** (b); the doublet potential energy surface for the reaction of Co(II)(BDPP) with O_2 as a function of the Co–O_2 bond distance obtained by CASSCF(13,9)/NEVPT2 computations. The dot lines denote diabatic potential curves, namely, the magenta line denotes a doublet Co^{II}–O$_2$ complex, interpreted as an $S_{Co}=\frac{3}{2}$ Co^{II} center antiferromagnetically coupled (FC) with a triplet O_2 ligand (S_{O_2} = 1); the crimson line denotes a doublet Co^{III}–O$_2$$^{-\bullet}$ complex, interpreted as an S_{Co} = 0 Co^{III} ion interacting with a doublet O$_2$$^{-\bullet}$ ligand $\left(S_{O_2^{-}\bullet}=\frac{1}{2}\right)$; the black line denotes the $S_t=\frac{1}{2}$ adiabatic curve; spin density and Löwdin and Mulliken (in parentheses) spin populations on the Co center and the O_2 ligand calculated for complexes ^{2}**C** (Co(II)(BDPP) + O^2), ^{2}**D** and ^{2}**2** on the reaction trajectory are shown at the bottom, yellow and red denote negative and positive spin density, respectively, and local spin populations are also listed in the ESI† (c); hydrogen atoms are omitted for clarity.

high spin Co(II) center $\left(S_{\mathrm{Co}} = \frac{3}{2}\right)$ and a triplet O_2 ligand (S_{O_2} = 1) is constantly uphill as the Co–O_2 bond length decreases. Furthermore, starting from the Co–O_2 distance of 2.50 Å, we could find another diabatic potential curve (crimson line) that is best described as a low spin Co(III) ion (S_{Co} = 0) interacting with a doublet superoxide radical $\left(S_{O_2^{-}\bullet} = \frac{1}{2}\right)$. Its energy first decreases for the Co–O_2 distance descending from 2.50 Å to 1.90 Å and then increases for the even shorter Co–O_2 distances; hence, a local minimal (^{2}**2**) is located at the Co–O_2 length of ~1.90 Å. Two diabatic potential curves interact in the vicinity of the Co–O_2 distance being 2.40 Å and generate an avoided crossing with a barrier of 24.7 kcal mol^{-1} for the O_2 binding reaction affording complex ^{2}**2**. Moreover, the entire process is slightly endothermic by 8.4 kcal mol^{-1}. In analogy to the O_2 association yielding ^{7}**1**, our *ab initio* computations likely overestimate the barrier and the driving force, because experimentally complex ^{2}**2** is stable at low temperatures (<193 K) but releases O_2 upon elevating the temperature.[22]

CASSCF(13,9) calculations of complex ^{2}**C** produce a predominant electron configuration of $\mathrm{d}_{xz}{}^2\mathrm{d}_{yz}{}^2\mathrm{d}_{xy}{}^1\mathrm{d}_{x^2-y^2}{}^1\mathrm{d}_{z^2}{}^1\pi_{\mathrm{ip}}{}^2\pi_{\mathrm{op}}{}^2\pi_{\mathrm{ip}}^{*1}\pi_{\mathrm{op}}^{*1}$ accounting for 80% of the wavefunction. As demonstrated in Fig. 4, the computed spin density plot exhibits a double-layer donut shape of the O_2 ligand, which implies that unpaired electrons equally populate its π_{ip}^* and π_{op}^* orbitals. Therefore, both findings suggest that complex ^{2}**C** is best interpreted as a high spin Co(II) center $\left(S_{\mathrm{Co}} = \frac{3}{2}\right)$ antiferromagnetically coupled to a triplet O_2 ligand (S_{O_2} = 1) yielding an overall $S_t = \frac{1}{2}$ ground state. Again, we constituted two-fragment spin eigenfunctions using CGCs to interpret this wavefunction and it reads $\left|\frac{1}{2}, \frac{1}{2}\right\rangle = \frac{1}{\sqrt{2}}\left|\frac{3}{2}, \frac{3}{2}\right|1, -1\right\rangle - \frac{1}{\sqrt{3}}\left|\frac{3}{2}, \frac{1}{2}\right|1, 0\right\rangle + \frac{1}{\sqrt{6}}\left|\frac{3}{2}, -\frac{1}{2}\right|1, 1\right\rangle$. This spin eigenfunction gives $\hat{S}_z$ expectation values of $\frac{5}{6}$ and $-\frac{1}{3}$ for the Co(II) center and the O_2 ligand, respectively. Indeed, both values are in line with the computed spin populations, which confirms the proposed electronic-structure assignment.

On the other hand, *ab initio* calculations suggest that complex ^{2}**2** features a leading configuration of $\mathrm{d}_{xz}{}^2\mathrm{d}_{yz}{}^2\mathrm{d}_{xy}{}^2\mathrm{d}_{x^2-y^2}^0\left(\mathrm{d}_{z^2} - \pi_{\mathrm{ip}}^*\right)^0\pi_{\mathrm{ip}}{}^2\pi_{\mathrm{op}}{}^2\left(\pi_{\mathrm{ip}}^* + \mathrm{d}_{z^2}\right)^2\pi_{\mathrm{op}}^{*1}$ (95%). Clearly, its electronic structure is best described as a low spin Co(III) center (S_{Co} = 0) bound to a doublet superoxo ligand $\left(S_{O_2^{-}\bullet} = \frac{1}{2}\right)$, congruent with the computed spin density and spin populations of 0.01 for the Co center and of 0.98 for the O_2 moiety as demonstrated in Fig. 4.

Regarding the O_2 binding process furnishing ^{2}**2**, as the Co–O_2 distance decreases from 4.50 Å to 2.30 Å (magenta curve), the wavefunction steadily acquires multireference character with three dominant electron configurations of $\mathrm{d}_{xz}{}^2\mathrm{d}_{yz}{}^2\mathrm{d}_{xy}{}^1\mathrm{d}_{x^2-y^2}{}^1\left(\mathrm{d}_{z^2} - \pi_{\mathrm{ip}}^*\right)^1\pi_{\mathrm{ip}}{}^2\pi_{\mathrm{op}}{}^2\left(\pi_{\mathrm{ip}}^* + \mathrm{d}_{z^2}\right)^1\pi_{\mathrm{op}}^{*1}$, $\mathrm{d}_{xz}{}^2\mathrm{d}_{yz}{}^2\mathrm{d}_{xy}{}^1\mathrm{d}_{x^2-y^2}{}^1\left(\mathrm{d}_{z^2} - \pi_{\mathrm{ip}}^*\right)^0\pi_{\mathrm{ip}}{}^2\pi_{\mathrm{op}}{}^2\left(\pi_{\mathrm{ip}}^* + \mathrm{d}_{z^2}\right)^2\pi_{\mathrm{op}}^{*1}$, and $\mathrm{d}_{xz}{}^2\mathrm{d}_{yz}{}^2\mathrm{d}_{xy}{}^1\mathrm{d}_{x^2-y^2}{}^1\left(\mathrm{d}_{z^2} - \pi_{\mathrm{ip}}^*\right)^2\pi_{\mathrm{ip}}{}^2\pi_{\mathrm{op}}{}^2\left(\pi_{\mathrm{ip}}^* + \mathrm{d}_{z^2}\right)^0\pi_{\mathrm{op}}^{*1}$. These three electron configurations differ in their varying occupation numbers in $\pi_{\mathrm{ip}}^* + \mathrm{d}_{z^2}$ and $\mathrm{d}_{z^2} - \pi_{\mathrm{ip}}^*$ orbitals that describe the covalent interaction between the Co(II) center and O_2 ligand as depicted in Fig. 1. During this process, the weights of the last two terms rise from 0% to 34% and 17%, respectively, which comes at the price of the percentage of the first one that lowers from 80% to 22%, perhaps signaling the increased Co–O_2 bonding strength. However, the electronic structure of ^{2}**D** is similar to that of ^{2}**C** as evidenced by the comparable spin density and spin populations computed for both species, which suggests that the Co–O_2 covalent interaction is rather weak. As the Co–O_2 distance further declines, a one-electron transfer from the Co(II) center to the O_2 ligand occurs around the avoided crossing region concurrent with a rapid adjustment of the electronic structure of the Co(III) center furnishing complex ^{2}**2**.

The doublet potential energy surface of the O_2 association process yielding ^{2}**2** is also constructed by two diabatic potential curves, one represents the reactant complex containing a high spin Co(II) center $\left(S_{\mathrm{Co}} = \frac{3}{2}\right)$ antiferromagnetically coupled to a triplet O_2 ligand (S_{O_2} = 1) yielding an overall $S_t = \frac{1}{2}$ ground state, and the other describes the product complex consisting of a low spin Co(III) ion (S_{Co} = 0) interacting with a doublet superoxide radical $\left(S_{O_2^{-}\bullet} = \frac{1}{2}\right)$. For the reaction of Co(II)(BDPP) with O_2, the emergence of the avoided crossing region suggests that no intermediate other than ^{2}**2** can be observed and that the Co(II)–O_2 adduct does not exist, consistent with the experimental findings.[22]

For O_2 binding on Fe(II)(BDPP) and Co(II)(BDPP), our *ab initio* calculations show that the former process has a lower barrier of 13.6 kcal mol^{-1} to ^{7}**1** than the latter (24.7 kcal mol^{-1}) to ^{2}**2**. This theoretical prediction is congruent with the experimental observation that the generation of ^{7}**1** is much faster than that of ^{2}**2**.[20,22] Furthermore, both transformations feature an avoided crossing that realizes one-electron transfer from a divalent metal center to O_2 and furnishes a trivalent metal center and a superoxo ligand as the final product; consequently, the divalent–O_2 adduct cannot be formed.

As elaborated in the section of Introduction, except one case, reactions of O_2 with a wide variety of Fe(II) and Co(II) precursors reported thus far all generate Fe(III) or Co(III) superoxo products, which intimates that the avoided crossing found for the O_2 addition processes on Fe(II)(BDPP) and Co(II)(BDPP) occurs in those transformations as well. In fact, the O_2 association to related Mn(II)(BDPP) also produces a Mn(III)–$O_2^{-\bullet}$ complex, instead of Mn(II)–O_2.[29] Likewise, the treatment of a series of Cu(I) species including [Cu(NH$_2$-TMPA)]$^+$ (TMPA = tris-methyl pyridine amine),[73] [Cu(TMG$_3$tren)]$^+$ (TMG$_3$tren = tris(tetramethylguanidino)tren)[74] and [Cu(Ar$_3$-TMPA)]$^+$

(Ar = tpb, dpb and dtbpb)[75] with O_2 invariably affords Cu(II)–$O_2^{-\bullet}$, whereas the authenticated O_2 adduct, Cu(I)–O_2, is yet to be disclosed. For more reactions of O2 and metal complexes affording superoxo adducts, readers may refer to review articles.[76–80] However, the reaction of O_2 with Y257F-HPCA was proposed to furnish Fe(II)–O_2 rather than Fe(III)–$O_2^{-\bullet}$. This proposition was solely based on ^{57}Fe Mössbauer measurements that give an unambiguous assignment of the Fe oxidation state, but the detailed information about the exact valence state of the O_2 ligand remains lacking. Therefore, thorough experimental research is required to verify the advocated electronic-structure assignment and disprove and/or substantiate our theoretical prediction.

Comments on DFT computations

For a given state distinguished by a total spin of S, M_s, its spin projection along the z axis, possesses $2S + 1$ values $(-S, -S + 1, \ldots, S - 1, S)$ and constitutes $2S + 1$ microstate labelled as $|S,M_s\rangle$. Among them, only $|S,S\rangle$ and $|S, -S\rangle$ could be represented by a single Slater determinant, whereas others have to be constructed as a linear combination of a series of Slater determinants, all having the same eigenvalue of M_s with respect to $\hat{S}_z$, in order to be the eigenfunctions of $\hat{S}^2$. Therefore, single-Slater-determinant approaches such as DFT could only deal with $|S,S\rangle$ and $|S, -S\rangle$. Both are equivalent except for the different eigenvalue for $\hat{S}_z$; hence, typically merely $|S,S\rangle$ called the standard component is computed. A representative example is complex ^{2}**2** in Fig. 5, for which the spin populations of Co and O_2 from B3LYP calculations with $\langle\hat{S}^2\rangle = 0.76$ are -0.02 and 1.00, respectively, congruent with the anticipated spin eigenfunction of $\left|\frac{1}{2},\frac{1}{2}\right\rangle$.

For systems featuring magnetic couplings of two fragments with their respective spins of S_1 and S_2, the resulting state may possess a total spin $S_t = S_1 - S_2, S_1 - S_2 + 1, \ldots, S_1 + S_2, (S_1 > S_2)$ according to the well-established rule of angular momentum addition. As elaborated above, the spin wavefunction, $|S,M\rangle$, could be built up by the spin eigenfunctions of two constituent fragments, $|S_1,M_1\rangle$ and $|S_2,M_2\rangle$. Of note, as required by the symmetry of CGCs, $M = M_1 + M_2$. Geometrically, this means that the z component of the vector sum of two angular momenta is equal to the algebraic sum of their z components. For ferromagnetic coupling with $S_t = S_1 + S_2$, the spin eigenfunction of its standard component, $|S_1 + S_2, S_1 + S_2\rangle$, could also be represented by a single Slater determinant constructed by the combination of two single Slater determinants distinguished by $|S_1,S_1\rangle$ and $|S_2,S_2\rangle$ for the two components into one. Thus, such systems can be properly treated with DFT, for instance, the septet reaction of O_2 with Fe(II)(BDPP). As demonstrated in Fig. 5, the spin populations on the Fe center and O_2 ligand estimated by B3LYP computations for ^{7}**A** (3.62 for Fe(II) and 1.99 for O_2) and ^{7}**1** (4.10 for Fe(III) and 1.20 for $O_2^{-\bullet}$) are all in line with those (3.86 for Fe(II) and 2.00 for O_2 in ^{7}**A**, 4.74 for Fe(III) and 1.03 for $O_2^{-\bullet}$ in ^{7}**1**) derived from CASSCF(12,9) calculations. Moreover, the computed $\hat{S}^2$ expectation values of $\langle\hat{S}^2\rangle = 12.00$ for ^{7}**A** and $\langle\hat{S}^2\rangle = 12.00$ for ^{7}**1** indicate that both B3LYP solutions are devoid of considerable spin contamination and are eigenfunctions of $\hat{S}^2$ having well-defined energies.

The situation is distinctly different for systems involving antiferromagnetic couplings where the resulting state has a total spin of $S_t < S_1 + S_2$, and the wavefunction of its standard component, $|S_t,S_t\rangle$, cannot be represented as a single determinant but has to be constructed as a linear combination of a range of Slater determinants with the eigenvalue of $\hat{S}_z$ being S_t to fulfill the requirement of spin symmetry. Therefore, in principle, DFT cannot be used to compute the electronic structures of such systems.

For one particular case with $S_t = S_1 - S_2$, its standard component $|S_1 - S_2, S_1 - S_2\rangle$ again should be built up as a linear combination of $|S_1,S_1|S_2, -S_2\rangle$, $|S_1,S_1 - 1|S_2, -S_2 + 1\rangle$, $\ldots$, all featuring the same the $\hat{S}_z$ eigenvalue of $S_1 - S_2$. Importantly, the first one could be described as a single Slater determinant formed by the combination of two single Slater determinants characterized by $|S_1,S_1\rangle$ and $|S_2, -S_2\rangle$ for the two constituent fragments into one. Broken symmetry formalism exploits this feature and approximate $|S_1 - S_2,S_1 - S_2\rangle$ as $|S_1,S_1|S_2, -S_2\rangle$, which means just choosing the first component from the above series. Consequently, the resulting solution is no longer the eigenfunction of $\hat{S}^2$ and spin density and spin populations derived from broken symmetry calculations are not correct. Generally speaking, nonnegligible spin contamination should be regarded as a characteristic of broken symmetry solutions that can be used to differentiate it from usual "spin-pure" solution discussed above. A case in point is complex ^{2}**C** where spin populations of 2.59 for Co(II) and -1.99 for O_2 provided by broken symmetry B3LYP calculations are in line with the expected values for $\left|\frac{3}{2},\frac{3}{2}\middle|1,-1\right\rangle$ (Fig. 5). These erroneous values differ significantly from those (1.58 for Co(II) and -0.66 for O_2) derived from CASSCF(13,9) calculations, but nevertheless indicate that the local spins of the Co(II) center and the O_2 ligand are $\frac{3}{2}$ and 1, respectively, thus yielding a qualitatively correct bonding description of complex ^{2}**C**. However, this DFT solution suffers from unacceptable spin contamination with $\langle\hat{S}^2\rangle = 2.77$. As a consequence, its energy is not

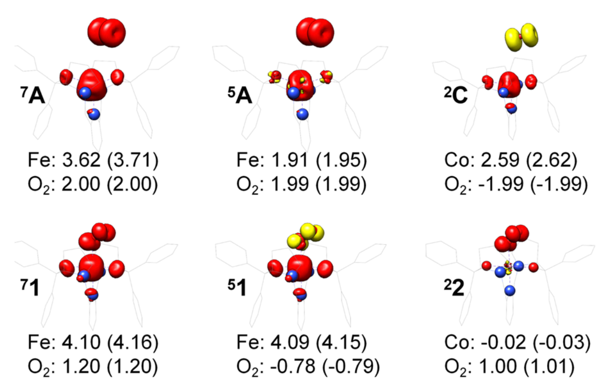

Fig. 5 Spin density and Löwdin and Mulliken (in parentheses) spin populations for the metal center and the O_2 ligand from DFT calculations; ligand atoms are omitted for clarity.

reliable because it is not the eigenfunction of the Hamiltonian operator, $\hat{H}$, either. As shown in Fig. 5, complex ^{5}**1** also belongs to this category.

While for other resulting state with $S_1 - S_2 < S_t < S_1 + S_2$, its standard component cannot be approximately by a single Slater determinant any more. For example, for $S_t = S_1 + S_2 - 1$, the standard component characterized by $|S_1 + S_2 - 1, S_1 + S_2 - 1\rangle$ should be constructed as a linear combination of the wavefunction distinguished by $|S_1,S_1 - 1|S_2,S_2\rangle$ and $|S_1,S_1|S_2,S_2 - 1\rangle$. As elaborated above, both $|S_1,S_1 - 1\rangle$ and $|S_2,S_2 - 1\rangle$ cannot be represented by a single Slater determinant; hence, neither can $|S_1,S_1 - 1|S_2,S_2\rangle$ nor $|S_1,S_1|S_2,S_2 - 1\rangle$. Thus, DFT completely fails for this kind of systems as exemplified by complex ^{5}**A**. As depicted in Fig. 5, spin populations on Fe(II) of 1.90 and O_2 of 1.99 for O_2 erroneously predicted by DFT calculations indicate that the converged B3LYP solution is best interpreted as a triplet Fe(II) center ($S_{Fe} = 1$) ferromagnetically coupled to a triplet O_2 ligand ($S_{O_2} = 1$); therefore, the local spins of Fe and O_2 are qualitatively wrong.

In summary, only systems possessing two ferromagnetically coupled fragments, DFT calculations can be used to compute their electronic structures and spin density and spin populations and give reliable energies; otherwise, DFT computations in principle produce incorrect electronic structures and spin density and spin populations. For states with $S_t = S_1 - S_2$, the electronic structure can be approximately computed by invoking broken symmetry formalism in the framework of DFT calculations. But interpreting the resulting spin density and populations requires particular caution. In particular, for open-shell singlets, the artificial spin density obtained from broken symmetry calculations is qualitatively incorrect, because there does not exist any spin density everywhere for diamagnetic systems irrespective of being closed-shell or open-shell singlets. For comparison, the potential energy surfaces computed by DFT are summarized in the ESI.†

Conclusions

CASSCF/NEVPT2 calculations were employed to explore the electronic-structure evolution over the course of O_2 binding on Co(II) and Fe(II) precursors affording Fe(III)–$O_2^{-\bullet}$ (**1**) and Co(III)–$O_2^{-\bullet}$ (**2**) complexes. For the former reaction on the septet and quintet potential surfaces, starting complex ^{7,5}**A** is best formulated as a high spin Fe(II) center ($S_{Fe} = 2$) ferromagnetically or magnetically coupled with a triplet O_2 ligand ($S_{O_2} = 1$), while product ^{7,5}**1** consists of a high spin Fe(III) center $\left(S_{Fe} = \frac{5}{2}\right)$ ferromagnetically or antiferromagnetically coupled a superoxo ligand $\left(S_{O_2^{-\bullet}} = \frac{1}{2}\right)$. Regarding the latter reaction in an $S = \frac{1}{2}$ state, initial complex ^{2}**C** could be best characterized as a high spin Co(II) center $\left(S_{Co} = \frac{3}{2}\right)$ antiferromagnetically coupled to a triplet O_2 ligand ($S_{O_2} = 1$), while O_2 adduct ^{2}**2** contains a low spin Co(III) center ($S_{Co} = 0$) interacting with a superoxo ligand $\left(S_{O_2^{-\bullet}} = \frac{1}{2}\right)$. As O_2 steadily approaches the divalent metal center, the diabatic energy curve of M(II)–O_2 constantly rises in energy and interacts with that of M(III)–$O_2^{-\bullet}$ at a M–O_2 distance of around ∼2.40 Å. This interaction generates an avoided crossing that effects a spontaneous single-electron transfer from the divalent metal center to the incoming O_2 ligand, thereby leading to M(III)–$O_2^{-\bullet}$ as the final product and ruling out the possibility of formation of a *bona fide* M(II)–O_2 complex. This view has been used to explain the reaction outcomes of related O_2 association processes.

To extract electronic-structure information from complicated multireference wavefunctions, we constructed two-fragment spin eigenfunctions with CGCs to rationalize computed spin density and fragment spin populations on metal centers and O_2 moieties and deduced corrected electronic-structure formulations. This approach is complementary to usual VB analyses as demonstrated by applications of both methods to analyze the electronic-structure of O_2 adduct ^{5}**1**. This species features antiferromagnetic coupling of a high spin Fe(III) center $\left(S_{Fe} = \frac{5}{2}\right)$ and a superoxo ligand $\left(S_{O_2^{-\bullet}} = \frac{1}{2}\right)$; however, directly reading out electron configurations of the resulting authenticated multireference wavefunctions hardly gains any chemically sensible bonding information.

For systems involving metal–ligand or metal–metal antiferromagnetic couplings with $S_t = S_1 - S_2$, DFT calculations, despite giving a qualitatively right electronic structure, invariably suffer from spin contamination. Consequently, the resulting spin density and spin populations are not reliable. Furthermore, DFT fails completely for systems with $S_1 - S_2 < S_t < S_1 - S_2$ in predicting qualitatively correct electronic structures. Only for ferromagnetically coupled systems with $S_t = S_1 + S_2$, DFT is able to give exact electronic structures and energies.

Author contributions

S. Y. conceived the presented idea. P. Z. performed the computations and wrote the original draft. S. Y. and W. L. reviewed and edited the final draft. All authors discussed the results and contributed to the final manuscript.

Data availability

The data supporting this article have been included as part of the ESI.†

Conflicts of interest

There are no conflicts to declare.

Acknowledgements

The work conducted in Dalian was supported by the National Key R&D Program of China (No. 2021YFA1502803), the National

Natural Science Foundation of China (92161204) and the DaIian Institute of Chemical Physics, Chinese Academy of Sciences (Grant: DICP I202312). W. L. is grateful for the financial support from the Ministry of Science and Technology of Taiwan (MOST 111-2113-M-003-008-MY3 to W.-Z. L.). We are indebted to Mr Haowei Chen for his helpful discussions.

Notes and references

1 M. Costas, M. P. Mehn, M. P. Jensen and L. Que Jr, *Chem. Rev.*, 2004, **104**, 939.

2 E. G. Kovaleva and J. D. Lipscomb, *Nat. Chem. Biol.*, 2008, **4**, 186.

3 E. I. Solomon, D. E. Heppner, E. M. Johnston, J. W. Ginsbach, J. Cirera, M. Qayyum, M. T. Kieber-Emmons, C. H. Kjaergaard, R. G. Hadt and L. Tian, *Chem. Rev.*, 2014, **114**, 3659.

4 C. E. Elwell, N. L. Gagnon, B. D. Neisen, D. Dhar, A. D. Spaeth, G. M. Yee and W. B. Tolman, *Chem. Rev.*, 2017, **117**, 2059.

5 X. Huang and J. T. Groves, *Chem. Rev.*, 2017, **118**, 2491.

6 A. J. Jasniewski and L. Que, Jr., *Chem. Rev.*, 2018, **118**, 2554.

7 L. Pauling and C. D. Coryell, *Proc. Natl. Acad. Sci. U. S. A.*, 1936, **22**, 210.

8 B. A. Springer, S. G. Sligar, J. S. Olson and G. N. Phillips Jr., *Chem. Rev.*, 1994, **94**, 699.

9 K. Shikama, *Chem. Rev.*, 1998, **98**, 1357.

10 J. E. Baldwin and M. Bradley, *Chem. Rev.*, 1990, **90**, 1079.

11 P. L. Roach, I. J. Clifton, V. Fülöp, K. Harlos, G. J. Barton, J. Hajdu, I. Andersson, C. J. Schofield and J. E. Baldwin, *Nature*, 1995, **375**, 700.

12 P. L. Roach, I. J. Clifton, C. M. H. Hensgens, N. Shibata, C. J. Schofield, J. Hajdu and J. E. Baldwin, *Nature*, 1997, **387**, 827.

13 M. M. Mbughuni, M. Chakrabarti, J. A. Hayden, E. L. Bominaar, M. P. Hendrich, E. Münck and J. D. Lipscomb, *Proc. Natl. Acad. Sci. U. S. A.*, 2010, **107**, 16788.

14 L. Que Jr. and R. Y. N. Ho, *Chem. Rev.*, 1996, **96**, 2607.

15 E. I. Solomon, T. C. Brunold, M. I. Davis, J. N. Kemsley, S. Lee, N. Lehnert, F. Neese, A. J. Skulan, Y. Yang and J. Zhou, *Chem. Rev.*, 2000, **100**, 235.

16 R. A. Baglia, J. P. T. Zaragoza and D. P. Goldberg, *Chem. Rev.*, 2017, **117**, 13320.

17 S. Yadav, V. Yadav, M. A. Siegler, P. Moënne-Loccoz, G. N. L. Jameson and D. P. Goldberg, *J. Am. Chem. Soc.*, 2024, **146**(12), 7915.

18 C. Winslow, H. Lee, M. J. Field, S. J. Teat and J. Rittle, *J. Am. Chem. Soc.*, 2021, **143**(34), 13686.

19 M. N. Blakely, M. A. Dedushko, P. C. Y. Poon, G. Villar-Acevedo and J. A. Kovacs, *J. Am. Chem. Soc.*, 2019, **141**(5), 1867.

20 J. Sacramento, T. Albert, M. Siegler, P. Moënne-Loccoz and D. P. Goldberg, *Angew. Chem., Int. Ed.*, 2022, **61**, e202111492.

21 C. Chiang, S. T. Kleespies, H. D. Stout, K. K. Meier, P. Li, E. L. Bominaar, L. Que Jr., E. Münck and W. Lee, *J. Am. Chem. Soc.*, 2014, **136**, 10846.

22 P. Zhang, Y. Tian, Z. Wang, W. Lee and S. Ye, *Chem. – Eur. J.*, 2024, **30**, e202400336.

23 C. Wang, H. Chang, Y. Lai, H. Fang, C. Li, H. Hsu, Z. Li, T. Lin, T. Kuo, F. Neese, S. Ye, Y. Chiang, M. Tsai, W. Liaw and W. Lee, *J. Am. Chem. Soc.*, 2016, **138**, 14186.

24 A. J. Fielding, J. D. Lipscomb and L. Que Jr., *J. Am. Chem. Soc.*, 2012, **134**, 796.

25 F. A. Walker and J. Bowen, *J. Am. Chem. Soc.*, 1985, **107**, 7632.

26 J. B. Gordon, A. C. Vilbert, M. A. Siegler, K. M. Lancaster, P. Moënne-Loccoz and D. P. Goldberg, *J. Am. Chem. Soc.*, 2019, **141**(5), 3641.

27 P. Kumar, S. V. Lindeman and A. T. Fiedler, *J. Am. Chem. Soc.*, 2019, **141**, 10984.

28 A. Huber, L. Müller, H. Elias, R. Klement and M. Valko, *Eur. J. Inorg. Chem.*, 2005, 1459.

29 J. Yang, P. Li, X. Li, L. Xie, N. Wang, H. Lei, C. Zhang, W. Zhang, Y.-M. Lee, W. Zhang, R. Cao, S. Fukuzumi and W. Nam, *Angew. Chem., Int. Ed.*, 2022, **61**, e202208143.

30 Y. Lin, H. Hinrika Cramer, M. van Gastel, Y. Tsai, C. Chu, T. Kuo, I. Lee, S. Ye, E. Bill and W. Lee, *Inorg. Chem.*, 2019, **58**, 9756.

31 H. Pan, H. Chen, Z. Wu, P. Ge, S. Ye, G. Lee and H. Hsu, *JACS Au*, 2021, **1**, 1389.

32 E. G. Kovaleva, M. B. Neibergall, S. Chakrabarty and J. D. Lipscomb, *Acc. Chem. Res.*, 2007, **40**, 475.

33 S. M. Adam, G. B. Wijeratne, P. J. Rogler, D. E. Diaz, D. A. Quist, J. J. Liu and K. D. Karlin, *Chem. Rev.*, 2018, **118**, 10840.

34 E. G. Kovaleva and J. D. Lipscomb, *Science*, 2007, **316**, 453.201.

35 M. M. Mbughuni, K. K. Meier, E. Munck and J. D. Lipscomb, *Biochemistry*, 2012, **51**, 8743.

36 M. Radon and K. Pierloot, *J. Phys. Chem. A*, 2008, **112**, 11824.

37 H. Chen, M. Ikeda-Saito and S. Shaik, *J. Am. Chem. Soc.*, 2008, **130**, 14778.

38 S. Shaik and H. Chen, *J. Biol. Inorg. Chem.*, 2011, **16**, 841.

39 H. Chen, K. Cho, W. Lai, W. Nam and S. Shaik, *J. Chem. Theory Comput.*, 2012, **8**, 915.

40 G. J. Christian, S. Ye and F. Neese, *Chem. Sci.*, 2012, **3**, 1600.

41 S. Ye, C. Riplinger, A. Hansen, C. Krebs, J. M. Bollinger, Jr. and F. Neese, *Chem. – Eur. J.*, 2012, **18**, 6555.

42 K. P. Jensen, B. O. Roos and U. Ryde, *J. Inorg. Biochem.*, 2005, **99**, 45.

43 K. P. Kepp, *ChemPhysChem*, 2013, **14**, 3551.

44 Q. M. Phung and K. Pierloot, *Phys. Chem. Chem. Phys.*, 2018, **20**, 17009.

45 L. Noodleman, *J. Chem. Phys.*, 1981, **74**, 5737.

46 J. Ribas-Arino and J. J. Novoa, *Chem. Commun.*, 2007, 3160.

47 P. Malmqvist and B. O. Roos, *Chem. Phys. Lett.*, 1989, **155**, 189.

48 C. Angeli, R. Cimiraglia and J.-P. Malrieu, *J. Chem. Phys.*, 2002, **117**, 9138.

49 C. Angeli, R. Cimiraglia, S. Evangelisti, T. Leininger and J. P. Malrieu, *J. Chem. Phys.*, 2001, **114**, 10252.

50 M. E. Rose, *Elementary theory of angular momentum*, Dover Publications Inc., New York, 1957.

51 A. D. Becke, *J. Chem. Phys.*, 1993, **98**, 5648.

52 C. Lee, W. Yang and R. G. Parr, *Phys. Rev. B: Condens. Matter Mater. Phys.*, 1988, **37**, 785.

53 A. D. Becke, *Phys. Rev. A: At., Mol., Opt. Phys.*, 1988, **38**, 3098.

54 A. Schäfer, C. Huber and R. Ahlrichs, *J. Chem. Phys.*, 1994, **100**, 5829.

55 J. P. Perdew, K. Burke and M. Ernzerhof, *Phys. Rev. Lett.*, 1996, **77**, 3865.

56 F. Weigend and R. Ahlrichs, *Phys. Chem. Chem. Phys.*, 2005, **7**, 3297.

57 A. Schäfer, H. Horn and R. Ahlrichs, *J. Chem. Phys.*, 1992, **97**, 2571.

58 S. Kossmann and F. Neese, *J. Chem. Theory Comput.*, 2010, **6**, 2325.

59 K. Eichkorn, O. Treutler, H. Öhm, M. Häser and R. Ahlrichs, *Chem. Phys. Lett.*, 1995, **242**, 652.

60 F. Weigend, *Phys. Chem. Chem. Phys.*, 2006, **8**, 1057.

61 V. Barone and M. Cossi, *J. Phys. Chem. A*, 1998, **102**, 1995.

62 S. Grimme, S. Ehrlich and L. Goerigk, *J. Comput. Chem.*, 2011, **32**, 1456.

63 S. Grimme, J. Antony, S. Ehrlich and H. Krieg, *J. Chem. Phys.*, 2010, **132**, 154104.

64 C. Kollmar, K. Sivalingam, B. Helmich-Paris, C. Angeli and F. Neese, *J. Comput. Chem.*, 2019, **40**, 1463.

65 F. Weigend, *J. Comput. Chem.*, 2008, **29**, 167.

66 F. Neese, F. Wennmohs, U. Becker and C. Riplinger, *J. Chem. Phys.*, 2020, **152**, 224108.

67 H. Chen, P. Zhang and S. Ye, *Encyclopedia of Inorganic and Bioinorganic Chemistry*, 2024, DOI: **10.1002/9781119951438.eibc2883**.

68 C. Angeli, C. J. Calzado, C. de Graafcd and R. Caballol, *Phys. Chem. Chem. Phys.*, 2011, **13**, 14617.

69 C. Angelia, R. Cimiragliaa and J. Malrieu, *Mol. Phys.*, 2013, **111**, 1069.

70 L. Blancafort, P. Celani, M. J. Bearpark and M. A. Robb, *Theor. Chem. Acc.*, 2003, **110**, 92.

71 J. Malrieu, C. Angeli and R. Cimiraglia, *J. Chem. Educ.*, 2008, **85**, 150.

72 H. Chen, M. Ikeda-Saito and S. Shaik, *J. Am. Chem. Soc.*, 2008, **130**, 14778.

73 D. Maiti, H. C. Fry, J. S. Woertink, M. A. Vance, E. I. Solomon and K. D. Karlin, *J. Am. Chem. Soc.*, 2007, **129**, 26.

74 C. Wrtele, E. Gaoutchenova, K. Harms, M. C. Holthausen, J. Sundermeyer and S. Schindler, *Angew. Chem., Int. Ed.*, 2006, **45**, 3867.

75 S. Y. Quek, S. Debnath, S. Laxmi, M. van Gastel, T. Krämer and J. England, *J. Am. Chem. Soc.*, 2021, **143**(47), 19731.

76 R. Trammell, K. Rajabimoghadam and I. Garcia-Bosch, *Chem. Rev.*, 2019, **119**, 2954.

77 C. E. Elwell, N. L. Gagnon, B. D. Neisen, D. Dhar, A. D. Spaeth, G. M. Yee and W. B. Tolman, *Chem. Rev.*, 2017, **117**, 2059.

78 S. Fukuzumi and K. D. Karlin, *Coord. Chem. Rev.*, 2013, **257**, 187.

79 S. Hong, Y. Lee, K. Ray and W. Nam, *Coord. Chem. Rev.*, 2017, **334**, 25.

80 H. Noh and J. Cho, *Coord. Chem. Rev.*, 2019, **382**, 126.